Seismic interferometry facilitating the imaging of shallow shear-wave reflections hidden beneath surface waves

Liu, Jianhuan; Draganov, Deyan; Ghose, Ranajit

DOI
10.3997/1873-0604.2018013

Publication date
2018

Document Version
Accepted author manuscript

Published in
Near Surface Geophysics

Citation (APA)
Liu, J., Draganov, D., & Ghose, R. (2018). Seismic interferometry facilitating the imaging of shallow shear-wave reflections hidden beneath surface waves. *Near Surface Geophysics*, *16*(3), 372-382. https://doi.org/10.3997/1873-0604.2018013

Seismic interferometry facilitating the imaging of shallow shear-wave reflections hidden beneath surface waves

Jianhuan Liu[1], *Deyan Draganov*[1], *Ranajit Ghose*[1]
[1]*Department of Geoscience and Engineering, Delft University of Technology, The Netherlands. Email: j.liu-4@tudelft.nl; d.s.draganov@tudelft.nl; r.ghose@tudelft.nl*

Received September 2017, revision accepted April 2018

Abstract

High-resolution reflection seismics is a powerful tool that can provide the required resolution for subsurface imaging and monitoring in urban settings. Shallow seismic reflection data acquired in soil-covered sites are often contaminated by source-coherent surface waves and other linear moveout noises (LMON) that might be caused by, e.g., anthropogenic sources or harmonic distortion in vibroseis data. In the case of shear-wave seismic reflection data, such noises are particularly problematic as they overlap the useful shallow reflections. We have developed new schemes for suppressing such surface-wave noise and LMON while still preserving shallow reflections, which are of great interest to high-resolution near-surface imaging. We do this by making use of two techniques. First, we make use of seismic interferometry to retrieve predominantly source-coherent surface waves and LMON. We then adaptively subtract these dominant source-coherent surface waves and LMON from the seismic data in a separate step. We illustrate our proposed method using synthetic and field data. We compare results from our method with results from frequency–wavenumber (f-k) filtering. Using synthetic data, we show that our schemes are robust in separating shallow reflections from source-coherent surface waves and LMON even when they share very similar velocity and frequency contents, whereas f-k filtering might cause undesirable artefacts. Using a field shear-wave reflection dataset

characterised by overwhelming LMON, we show that the reflectors at a very shallow depth can be imaged because of significant suppression of the LMON due to the application of the scheme that we have developed.

Introduction

Engineering and environmental problems (e.g., sinkhole and groundwater-related issues) in urban areas often require highly detailed information about the subsurface structure in depth to a few metres. Among all available geophysical methods, for soil-covered areas, high-resolution reflection seismics using shear or S-waves (e.g., Pullan, Hunter and Neave 1990; Hasbrouck 1991; Ghose, Brouwer and Nijhof 1996; Ghose and Goudswaard 2004; Pugin *et al.* 2004; Krawczyk, Polom and Beilecke 2013; Konstantaki *et al*. 2014) is one of the few options to accomplish the target resolution of the subsurface in an urban setting. For example, using specialised seismic vibratory sources and shear waves, it has been possible in the past to achieve decimetre-scale seismic resolution in the near-surface soils (e.g., Ghose *et al.* 1996; Brouwer *et al.* 1997; Ghose *et al.,* 1998; Ghose 2002; Ghose and Goudswaard 2004).

However, most cities are located in soil-covered plains or Quaternary basins overlying consolidated bedrock (Sinsakul 2000; Haworth 2003). Shallow shear-wave reflection data acquired in such soil-covered sites is characterised by large amount of (dispersive) surface waves, which generally camouflage the very shallow reflections. The conventional techniques for suppression of surface waves, e.g., muting or spatial filtering (Yilmaz 2001) are ineffective or even detrimental to the target reflections in suppressing this source-generated noise, especially at near offsets. This is especially challenging in urban settings where the available source-receiver offset is often quite limited, and the

velocity and frequency content of the surface waves largely overlap with those of the target shear-wave reflections (unlike compressional wave reflections, which usually have much higher velocities than the surface waves). The first goal of the present research is, therefore, to reduce the surface waves due to the active source (source-coherent surface waves) and reveal the very shallow reflections in the recorded data using seismic interferometry (SI) and adaptive subtraction (AS).

Also, human activities (e.g., near-by traffic, construction works, or movement of people) are common during urban seismic surveys. When many such noise sources are excited simultaneously in the crossline direction, the traveltime from these noise sources to all receivers depends on the distance between these sources and the receivers. In the urban settings, such noise sources are mainly linearly distributed (such as in construction works or for moving vehicles), which means that the traveltime of such noise recorded in the shot gather will have a linear moveout. These arrivals exacerbate the already difficult problem of removing the surface waves generated by the active source used in the seismic survey. The source-incoherent surface waves can result in lower resolution in the imaging results and even lead to wrong seismic interpretation. The second motivation of the present study is to remove such source-incoherent surface waves using new processing schemes that we developed.

In this paper, we first present the steps for the implementation of our method. We then demonstrate the feasibility of our method in suppressing surface waves (from both inline and crossline directions) through modelling studies. Finally, we implement this method on a field dataset that is heavily contaminated by such noises.

Methodology

In our proposed method, we make use of SI to retrieve, at first, the dominant surface waves. The retrieved surface-wave energy is then adaptively subtracted from the data. For the horizontal arrivals (or dipping arrivals), they are retrieved at both causal and acausal time. Hence, they need to be isolated from the retrieved data in order to be further shifted back to the position of the physical arrivals, this is done by using singular value decomposition (SVD) filtering (for dipping arrivals, this involves linear move out correlation (LMO), SVD, and then inverse LMO). In this section, we first state how to implement seismic interferometry, adaptive subtraction, and SVD filtering separately. Then, a workflow is presented to describe how to assemble the separate operations to suppress different types of surface waves.

Seismic interferometry

SI refers to the process of estimating the full Green's functions (GF) between two receivers, by cross-correlating the recordings at the two receivers and stacking the crosscorrelations for all the sources (Wapenaar and Fokkema 2006). For the urban seismic survey using active sources, the retrieved GF $\hat{G}(\mathbf{X_A}, \mathbf{X_B}, \omega)$ between two receivers at $\mathbf{X_A}$ and $\mathbf{X_B}$ can be determined by (Halliday *et al.* 2007):

$$\hat{G}(\mathbf{X_A}, \mathbf{X_B}, \omega) + \hat{G}^*(\mathbf{X_A}, \mathbf{X_B}, \omega) \approx \sum_{n=1}^{N} \hat{G}^*(\mathbf{X_B}, \mathbf{X_i}, \omega)\hat{G}(\mathbf{X_A}, \mathbf{X_i}, \omega)\Delta\mathbf{X_i}, \quad (1)$$

where $\hat{G}(\mathbf{X_B}, \mathbf{X_i}, \omega)$ is a recording at receiver $\mathbf{X_B}$ from a source at $\mathbf{X_i}$ ($\hat{G}(\mathbf{X_A}, \mathbf{X_i}, \omega)$ is similar) represented in the frequency domain as indicated by the hat above G; the asterisk $(*)$ denotes the complex conjugation in the frequency domain, which corresponds to time-reversal in the time domain. N represents the number of active sources. If the sources were impulses, $\hat{G}$ would have represented an impulse response. For transient sources, $\hat{G}$ would represent a pressure or a particle-velocity recording convolved with the

autocorrelation of the source's time function. Via formula (1), we can turn the receiver at $\mathbf{X_B}$ into a virtual source. If we keep the receiver at $\mathbf{X_B}$ fixed and repeat the correlation and summation process for all the other receivers, the resulting retrieved result can approximate a virtual common-source gather with a virtual source located at $\mathbf{X_B}$. The theory of SI requires that the sources effectively surround the receivers and illuminate them homogeneously (Wapenaar and Fokkema 2006). When the receivers are at the surface, i.e., $\hat{G}$ represents a particle-velocity recording, active sources are required only in the subsurface (Wapenaar and Fokkema 2006). For the usual seismic exploration survey, e.g., for near-surface imaging, the active sources are present at the surface, where they are not required. Because of that, the retrieved result would contain physical arrivals – the direct and surface waves, but also pseudo-physical reflections and non-physical arrivals (e.g., Mikesell *et al.* 2009; Draganov, Heller, and Ghose 2012; King and Curtis 2012; Draganov *et al.* 2013). For a line survey, as all active sources are at the surface, they all will contribute to the retrieval of the direct and surface waves because all of them fall into the so-called stationary phase region (Snieder 2004). In this way, the result retrieved by SI will be dominated by surface waves, as they are the most energetic arrivals in a recording from active sources at the surface.

Adaptive subtraction

We use Figure 1 to illustrate the basic principles of AS. Figure 1a can be considered as a simple seismic data that consists of four events: one weak reflection at 100 ms, and another three high-amplitude surface-wave arrivals at 200 ms, 300 ms, and 400 ms, respectively. Figure 1b corresponds exactly to the surface-wave part of Figure 1a. By minimizing the difference between Figure 1a and Figure 1b, the surface waves in Figure

1a can be suppressed. This is done by estimating a shaping filter **f**, that can minimise the following objective function:

$$\mathbf{D}^{refl} = |\mathbf{D} - \mathbf{f}\mathbf{D}^{\mathbf{sw}}|_{min}, \quad (2)$$

where **D** is the raw data (Figure 1a), $\mathbf{D}^{\mathbf{sw}}$ contains the surface-wave part of **D** (Figure 1b), and $\mathbf{D}^{\mathbf{refl}}$ (Figure 1d) represents the data after suppression of the surface waves. We obtain this shaping filter **f** using the L1-norm, which follows the approach proposed by Guitton and Verschuur (2004). The convolution between the estimated shaping filter **f** and $\mathbf{D}^{\mathbf{sw}}$ (Figure 1b) leads to $\mathbf{fD}^{\mathbf{sw}}$ (Figure 1c), which will then be directly subtracted from **D** (Figure 1a), as expressed in equation (2), giving Figure 1d. Comparing Figure 1a and Figure 1d, we can see that the strong surface waves have been greatly reduced in Figure 1d, while the weak reflection at 100 ms is preserved.

In a field seismic reflection experiment, the exact location of surface waves recorded in the data (as in Figure 1b) are unknown. However, SI has proven to be a robust tool for estimating the surface-wave energy between receivers under certain survey geometry (e.g., Dong, He, and Schuster 2006; Halliday *et al.* 2007; Konstantaki *et al.* 2015). This means that the retrieved surface waves can then be regarded as an input for AS (as in Figure 1b), which will be adaptively subtracted from the data (as in Figure 1a).

SVD filtering

Multi-trace seismic data can be represented as a matrix **C** of size (m × n), where **m** denotes traces number and **n** denotes time samples. The SVD of matrix **C** is the factorization of **C** into the product of three matrices (Golub and van Loan 1996; Melo *et al.* 2013), which is $\mathbf{C}=\mathbf{U}\mathbf{S}\mathbf{V}^{\mathbf{t}}$, where **U** and **V** are the orthonormal left and right singular vectors, and matrix **S** is a diagonal matrix composed of the singular values of the original matrix **C**, in

descending order. By taking only the contribution of the first j singular values from **C**, a lower-rank approximation of **C** is obtained as: $\mathbf{C_j}=\mathbf{US_jV^t}$ (Eckart and Young 1936). Figure 2 illustrates how matrix **C** is approximated by its lower-rank matrix $\mathbf{C_j}$. Since SVD is a coherency-based technique (Bekara and van der Baan 2007), for the horizontal arrivals in Figure 2a, which show a high degree of coherency across the traces, they can be nicely isolated from the data by setting j to 2 (Figure 2d).

Modelling study 1: suppression of source-coherent surface waves

In Figure 3, we present the flowchart of the scheme for implementing SI+AS. Next, to demonstrate the effectiveness of SI+AS in the removal of different types of surface waves, which we typically confront in data from urban sites (where high-resolution seismic imaging is often of great value), we perform synthetic modelling studies. We consider a four-layer model (Figure 4). A 3-layered partially saturated top soil of total thickness of 12 m overlies the fully saturated soil below. We use an elastic finite-difference modelling scheme to generate synthetic common-source gathers (Thorbecke and Draganov 2011). The first source is positioned at 0 m and the last one at 30 m; the source spacing is 1 m. The array of receivers starts at 6 m and ends at 23.5 m, with a spacing between receivers of 0.5 m. Following the criteria of stability and numerical dispersion, we set the spatial grid of the model at 0.1 m and the time step of the modelling at 0.02 ms. To model shear wave, which we generated and recorded in the field data, the sources are excited along the inline direction and the vertical component of the data are used. The source signature is a 90-Hz Ricker wavelet. To suppress the reflections from the bottom and the side boundaries during the numerical modelling, we implement absorbing boundary conditions for these boundaries with a taper of 100 points.

Figure 5a shows an example of synthetic shot gathers for the source positioned at 15 m along the horizontal direction of the survey line. The surface waves, especially at far offset (see red ellipse in Figure 5a), mask the useful reflections. To reveal these reflections, we first make use of SI to retrieve a virtual common-source gather for a receiver located at 15 m (this receiver becomes the virtual source), following the steps described earlier in the methodology section. As shown in Figure 5b, the dominant surface waves in Figure 5a are retrieved well, while the retrieved reflections are significantly suppressed. We then adaptively subtract Figure 5b from Figure 5a, which results in Figure 5c. We analyse this result in Figure 6c, by comparing it with the data after conventional frequency-wavenumber (f-k) filtering (Figure 6b). We also show a reference shot gather (Figure 6d) without surface waves, modelled by replacing the free surface by a homogenous half space, to verify the effectiveness of these two techniques. As can be seen in Figure 6c, SI+AS does well in suppressing surface waves and hence two reflections with moveouts similar to the true reflections in Figure 6d can now be easily identified. For the used simple model, the f-k filtering also delivers good results and these two reflections can also be identified in Figure 6b; however, to avoid filtering out the reflection from the interface at 7 m, some surface-wave energy still leaked through the filter, as can be seen above that reflection.

To pick root-mean-square (RMS) velocities for stacking, we then carry out analysis using constant velocity stack (CVS) in the common midpoint (CMP) domain for the raw data, for the data after f-k filtering, and for the data after SI+AS. A selected representative part of the constant velocity stacked section is displayed in Figure 7. Because the surfaces waves present in the modelled data are characterized by moveout velocities similar to those of the useful reflection events, the alignment in the panels in

198 Figure 7a is ambiguous, making the picking of velocities inaccurate. Such ambiguity is
199 significantly reduced in Figure 7b, which shows CVS of the same data after f-k filtering.
200 As is shown in Figure 7b, the first event is flat in the first panel, while the second event
201 in third panel. Figure 7c is the CVS of this data after SI+AS. Comparing Figure 7b and
202 Figure 7c, we find that they both offer the same ease for picking the RMS velocity (0 ms-
203 170 m/s; 68 ms-210 m/s); these velocities will be used in the following stacking procedure.
204 However, Figure 7c shows a higher signal/noise ratio (S/N), when inspected carefully
205 (e.g., the blue ellipse). We will further compare in the stacked section this effectiveness
206 of suppressing different types of surface waves using f-k filtering and SI+AS schemes.
207 Figure 8a shows the stacked section obtained from the raw (unfiltered) active-
208 source data. In this stacked section, the inclined, high-amplitude surface waves (as the
209 one marked by the red ellipse) overlap the shallow shear-wave reflectors, making it
210 difficult to identify the latter in this area. However, due to the effective removal of the
211 surface waves by the application of SI+AS, in the resulting stacked section, shown in
212 Figure 8c, these same reflectors (red arrows) are much more continuous and clearer, and
213 thus quite easy to interpret. These reflectors are also correctly imaged in the stacked
214 section after f-k filtering, as is shown in Figure 8b. However, due to the close overlap
215 between surface waves and reflections in the f-k domain, it is difficult to design the f-k
216 filtering parameters to suppress sufficiently the surface waves. This leads to some leakage
217 of surface waves at certain shots. The artefacts in Figure 8b (see the red ellipse) are caused
218 by stacking of such leaked surface-wave energy. Note that the results in Figure 8b and 8c
219 exhibit apparent curving of the reflector at 7 m and lower amplitude of the reflector at 12
220 m on the left and right sides. This is caused by reduced stacking power in the CMP gathers
221 at those positions.

Modelling study 2: suppression of source-coherent surface waves and horizontal LMON

When conducting seismic surveys in urban environments, often, the recorded data contain surface waves that are not connected to the active source used in the survey. Such surface waves could be due to construction work, traffic passing close to the survey site, walking people, etc. These surface waves most likely would not be aligned with the survey line, but would be propagating in a crossline direction. This kind of surface-wave energy, unlike the surface waves generated by the active sources that we have discussed in the previous section, can be retrieved by the application of SI at times that are different from the times in the original active-source data, i.e., they will result in the retrieval of non-physical arrivals. Hence, such source-incoherent surface waves are hard to suppress from the original data using the procedure described above. Therefore, we consider a new approach to suppress this type of noise with the aim to make the previous SI+AS scheme work also in this situation.

When the noise source that generates the crossline surface waves is moving parallel to the survey line (e.g., from traffic passing by), and when the noise source is not too close to the receivers, the traveltime from the noise source to each receiver is almost the same. These arrivals will be characterized by nearly horizontal moveouts. To simulate this situation, we add surface waves with horizontal moveouts to our previously modelled data. In Figure 9a, we show an example of the resulting synthetic shot gather and mark areas containing this type of surface-wave energy by blue arrows. Figure 9b illustrates the result of the application of SI. We can see the dominant, retrieved non-physical surface-wave arrivals at both causal and acausal times – the horizontal arrivals at 0 ms

and at about +/- 100 ms. The other dominant, retrieved arrival is the source-coherent surface wave. Concentrating on the horizontal surface waves, we can see that in Figure 9b the horizontal arrivals (marked by blue arrows) are retrieved, but at times not coinciding with the times in the original data. This happens as the SI process effectively eliminates the common travel path shared by the two arrivals recorded at the two receivers. The SI process "recognizes" the earlier horizontal surface wave in Figure 9a as the arrival bearing the common travel path, and eliminates its time from the time of the later horizontal surface wave. To approximate both horizontal surface waves in Figure 9a as good as possible, we first apply SVD filtering to isolate them from the rest of the retrieved arrivals. We then use the acausal part of the isolated horizontal arrivals and shift them back to the physical time of the original horizontal surface waves in Figure 9a, which results in Figure 9c. The shifting is currently performed manually, but this process could be automated (beyond the scope of this work). We use the acausal part as it is free from interference from other arrivals. Looking at the retrieved inline surface waves (red arrow in Figure 9b), we see that its arrival time is consistent with the time of the original inline surface wave in Figure 9a (as should be expected from what was shown in the modelling study 1). For this retrieved arrival, we only need to isolate it from Figure 9b by subtracting the full isolated horizontal arrivals from Figure 9b and then taking the causal part of the result, which gives Figure 9d. Finally, these retrieved dominant arrivals (Figure 9c and Figure 9d) can now be adaptively subtracted one after the other from the original gather (Figure 9a), resulting in Figure 9e.

We also apply f-k filtering to Figure 9a in an attempt to suppress the inline surface waves and horizontal arrivals, the result of which is shown in Figure 10b. Comparing Figure 10b and Figure 10d, we see that two reflections can now be identified (red arrows

in Figure 10b), because of the removal of the inline surface waves after the f-k filtering. However, the performance of the f-k filtering in suppressing the horizontal arrivals is not good enough, as can be seen in Figure 10b, which leads to a large amount of those horizontal arrivals still remaining. On the contrary, those horizontal arrivals, along with inline surface waves, are significantly reduced in Figure 10c, leading to the emergence of two clear reflections (red arrows in Figure 10c).

Figure 11a is the stacked section obtained from the original data (containing the source-coherent and source-incoherent surface waves). Figures 11b and 11c show the stacked sections obtained from the same data after suppression of these two types of surface waves using f-k filtering and SI+AS schemes, respectively. The events (e.g., red rectangle in Figure 11a), caused by the stacking of source-incoherent surface-wave arrivals, can be wrongly interpreted as reflectors because of their continuity and clarity, which would be really problematic in urban seismic surveys. As visible in Figure 11b, the f-k filtering fails to suppress these artefacts sufficiently (e.g., red rectangle in Figure 11b) due to poor performance to suppress these horizontal arrivals without damaging the reflections. However, such artefacts are greatly reduced in Figure 11c – the reflectors are now correctly imaged and clearly interpretable. This shows that our approach is successful in the removal of most of the inline and crossline surface waves, with very little loss of the useful reflection energy.

Modelling study 3: suppression of source-coherent surface waves and dipping LMON

Often, there are other types of noise sources (than what has been discussed above) in urban environments, such as construction work taking place around the survey line.

Crossline surface waves caused by these sources may be characterized by dipping moveouts. To test if the surface-wave-suppression scheme that we propose in modelling study 2 could help also in the suppression of dipping crossline surface waves, we add source-incoherent dipping arrivals to our previously modelled data (modelling study 1). A resulting common-source gather is shown in Figure 12a, where the dipping surface-wave arrivals are marked by blue arrows. We first try to use f-k filtering to suppress the inline surface waves and dipping arrivals in Figure 12a, which produces the result shown in Figure 13b. In the f-k domain, these dipping arrivals fall inside the area where also most of reflection energy is located. To suppress these dipping arrivals using f-k filtering will also mean total loss of reflection energy, as can be seen in Figure 13b.

To reveal the true reflections, we apply an SI+AS scheme (as illustrated in Figure 12) similar to the one we used in the modelling study 2. The final common-source gather resulting from this scheme is displayed in Figure 13c. Two reflection events (red arrows in Figure 13c) have been revealed by the SI+AS procedure, and they can now be identified. Comparing the result in Figure 13c with the reference result shown in Figure 13d, we notice that the amplitudes of the revealed reflections in Figure 13c have been greatly weakened after the SI+AS procedure; nevertheless, they can be well-utilized in near-surface imaging.

Figure 14a shows the CMP stacked section using the data without surface-wave suppression. Two features (see the red rectangle in Figure 14a) with high amplitude and good continuity can be wrongly interpreted as reflectors. These features are due to the stacking of the dipping surface waves. These artefacts can be utterly misleading in the urban geophysical interpretation. Figure 14b shows the stacked section from the data after surface-wave suppression using f-k filtering. Because of the failure of the f-k filter to

suppress the dipping arrivals, artefacts (see the red rectangle in Figure 14b) caused by stacking these arrivals still remain in Figure 14b. The stacked section after surface-wave suppression using the SI+AS is shown in Figure 14c. Due to successful suppression of the dipping surface waves, the artefacts (e.g., red rectangle in Figure 14a) have nearly disappeared from Figure 14c. Therefore, we can now easily and correctly interpret the two deeper reflectors in Figure 14c.

Field-data example

In a high-resolution shear-wave reflection survey, the receiver line consisted of 120 horizontal-component geophones spaced at a 0.25 m interval, ranging from 42 to 71.75m. The geophones were oriented in the crossline direction. The receiver array was fixed during data collection, because of the limited available space in the survey area, which is a common constraint in urban settings. As a source, we used a high-frequency, electrodynamic horizontal vibrator (Ghose *et al.* 1996; Brouwer *et al.* 1997; Ghose and Goudswaard 2004; Ghose 2012) also oriented in the crossline direction. The source spacing was 1 m, starting from 42 m to 62m. As both the sources and the receivers are oriented in the crossline direction, we made use of shear-waves polarized in the crossline direction, i.e., SH-waves. The record length was 4 s. After vibroseis source signature deconvolution (Ghose 2002), we obtain common-source gathers with a length of 0.5 s. Figure 15a shows an example common-source gather after application of AGC (180 ms) and band-pass filtering (3-8-150-200 Hz). During the field work, due to the surface condition and source coupling, unfortunately harmonic distortion was significant in the compressed vibrator data, which showed up as LMON (blue ellipse in Figure 15a). This kind of noise, together with the source-coherent surface waves, is difficult to suppress

using traditional filtering techniques (e.g., f-k filtering, notch filtering), due to the very similar frequency content and moveout velocity as the informative reflection signals. This makes this dataset ideal for testing the efficacy of our newly developed scheme.

In order to restore the true reflectors from this severely noise-contaminated data, we apply the SI+AS scheme, as illustrated in modelling study 3, to the data shown in Figure 15a, with the main aim to suppress the dipping arrivals (see the area inside the blue ellipse). The result is shown in Figure 15c. Comparing the common-source gathers in Figure 15a and 15c, we can see that the dipping arrivals are significantly suppressed, and shallow reflections around 100 ms can now be identified clearly in Figure 15c. We interpret them as true reflections because they are crisp and they also show clear hyperbolic moveouts in shot gathers. For the same gather, after f-k filtering (Figure 15b) it is difficult to identify such shallow reflection events.

Figure 15d, 15e, 15f present the stacked section from the raw (unfiltered) field data, data after f-k filtering, and data after SI+AS, respectively. In Figure 15e, we see that there are many artefacts (example marked by red rectangle) caused by the f-k filtering. Without prior knowledge about the subsurface, the interpretation can become erroneous. However, in Figure 15f we can interpret a shallow reflector at around 100 ms two-way time, with a vertical resolution of less than 1m, because of the good quality stacking. This is due to the success of SI+AS scheme in suppressing LMON, while preserving the shallow shear-wave reflections.

Conclusions

High-resolution reflection seismics using shear waves can be very effective in subsurface investigations in densely populated soil-covered urban settings. However, a successful

application of the method can be hampered by the presence of source-coherent surface waves and/or other LMON in the field data, which camouflage the shallow shear-wave reflection events. We developed new schemes for the data-driven suppression of such surface- wave noise and LMON, while preserving the shallow reflections. Using numerical modelling data, we showed how a combination of SI and AS can significantly suppress the inline (source-coherent) surface waves and LMON and, hence, improve significantly the imaging of shallow subsurface structures. In comparison with f-k filtering, we demonstrate that our schemes are effective in separating reflections from source-coherent surface waves and LMON, even when they overlap greatly in the f-k domain. When applied to field shear-wave reflection data that are heavily contaminated by LMON, we found that crisp and clear shallow reflectors could be revealed, due to significant suppression of LMON as a result of the application of the newly developed SI + AS schemes.

ACKNOWLEDGEMENTS

The research of J.L. is supported by the China Scholarship Council (File No. 201604910851). The field data were acquired with the help of Dominique Ngan-Tillard, Joeri Brackenhoff, and Jens van den Berg. The seismic data were processed using a combination of Seismic Unix, ProMAX and software from the Delphi Consortium. The authors would like to thank the associate editor and two anonymous reviewers for their constructive comments that helped improve the manuscript.

References

Bekara M. and van der Baan M. 2007. Local singular value decomposition for signal enhancement of seismic data. *Geophysics* **72**, V59–V65.

Brouwer J., Ghose R., Helbig K. and Nijhof V. 1997. The improvement of geotechnical subsurface models through the application of S-wave reflection seismic exploration. Proc. *3rd Environ. Engineering Geophys. Soc Europ. Section Meeting,* 103-106.

Dong S., He R. and Schuster G. 2006. Interferometric predcition and least squares subtraction of surface waves. *SEG Technical Program Expanded Abstracts*. ***2006***, pp. 2783–2786.

Draganov D., Heller K. and Ghose R. 2012. Monitoring CO2 storage using ghost reflections retrieved from seismic interferometry. *International Journal of Greenhouse Gas Control* **11**, S35–S46, doi: 10.1016/j.ijggc.2012.07.026.

Draganov D., Ghose R., Heller K. and Ruigrok E. 2013. Monitoring of changes in velocity and Q in reservoirs using non-physical arrivals in seismic interferometry. *Geophysical Journal International* **192**, 699-709, doi: 10.1093/gji/ggs037.

Eckart C. and Young G. 1936. The approximation of one matrix by another of lower rank. *Psychometrika* **1**, 211–218.

Ghose R., Brouwer J. and Nijhof V. 1996. A portable S-wave vibrator for high-resolution imaging of the shallow subsurface. 58th EAGE Conference and Exhibition.

Ghose R., Nijhof V., Brouwer J., Matsubara Y., Kaida Y. and Takahashi T. 1998. Shallow to very shallow, high-resolution reflection seismic using a portable vibrator system. *Geophysics* **63**, 1295–1309.

Ghose R. 2002. High-frequency shear wave reflections from shallow subsoil layers using a vibrator source; sweep cross-correlation versus deconvolution with groundforce

414 derivative. *72nd Annual International Meeting, SEG, Expanded Abstracts*, pp. 1408-
415 1411.
416 Ghose R. and Goudswaard J. 2004. Integrating S-wave seismic-reflection data and cone
417 penetration test data using a multiangle multiscale approach. *Geophysics* **69**, 440–
418 459.
419 Ghose R. 2012. A microelectromechanical system digital 3C array seismic cone
420 penetrometer. *Geophysics* **77**, WA99-WA107.
421 Golub G. and van Loan C. 1996. *Matrix Computations*, The Johns Hopkins Univ. Press,
422 Baltimore, MD.
423 Guitton A. and Verschuur D.J. 2004. Adaptive subtraction of multiples using the L1-
424 norm. *Geophys. Prospect.* 52, 27–38.
425 Halliday D., Curtis A., Robertsson J. and van Manen D. 2007. Interferometric surface-
426 wave isolation and removal. *Geophysics* **72**, A69–A73.
427 Hasbrouck W. P. 1991. Four shallow-depth, shear-wave feasibility studeis. *Geophysics*
428 **56**, 1875-1885.
429 Haworth R.J. 2003. The shaping of Sydney by its urban geology. *Quaternary*
430 *International* **103**, 41–55.
431 King S. and Curtis A. 2012. Suppressing nonphysical reflections in Green's function
432 estimates using source-receiver interferometry. *Geophysics* **77**, Q15–Q25, doi:
433 10.1190/geo2011-0300.1.
434 Konstantaki L.A., Ghose R., Draganov D., Diaferia G. and Heimovaara T. 2014.
435 Characterization of a heterogeneous landfill using seismic and electrical resistivity
436 data. *Geophysics* **80**, EN13-EN25.
437 Konstantaki L.A., Draganov D., Ghose R. and Heimovaara T. 2015. Seismic

438 interferometry as a tool for improved imaging of the heterogeneities in the body of
439 a landfill. *Journal of Applied Geophysics* **122**, 28–39.
440 Krawczyk C., Polom U. and Beilecke T. 2013. Shear-wave reflection seismics as a
441 valuable tool for near-surface urban applications. *The Leading Edge* **32**, 256–263.
442 Melo G., Malcolm A., Mikesell T.D. and van Wijk K. 2013. Using SVD for improved
443 interferometric green's function retrieval, *Geophys. J. Int.* **194**(3), 1596–1612.
444 Mikesell D., van Wijk K., Calvert A. and Haney M. 2009. Virtual refraction: Useful
445 spurious energy in seismic interferometry. *Geophysics* **74**, A13–A17, doi:
446 10.1190/1.3095659.
447 Pugin A., Larson T., Sargent S., McBride J. and Bexfield C. 2004. Near-surface mapping
448 using SH-wave and P-wave seismic land-streamer data acquisition in Illinois, U.S.
449 *The Leading Edge* **23**, 677–682.
450 Pullan S. E., Hunter J. A. and Neave K. G. 1990. Shallow shear-wave reflection tests, 60th
451 Ann. Internat. Mtg., Soc. Expl. Geophys., Expanded Abstracts, 380-382,
452 Sinsakul S. 2000. Late Quaternary geology of the Lower Central Plain, Thailand. *Journal*
453 *of Asian Earth Sciences* **18**, 415–426.
454 Snieder R. 2004. Extracting the Green's function from the correlation of coda waves: A
455 derivation based on stationary phase. *Physical Review E* **69**, 46610.
456 Thorbecke J. and Draganov D. 2011. Finite-difference modeling experiments for seismic
457 interferometry. *Geophysics* **76**, H1–H18.
458 Wapenaar K. and Fokkema J. 2006 Green's function representations for seismic
459 interferometry. *Geophysics* **71**, SI33–SI46, doi: 10.1190/1.2213955.
460 Yilmaz Ö. 2001. Seismic data analysis: processing, inversion and interpretation of
461 seismic data: SEG, USA.

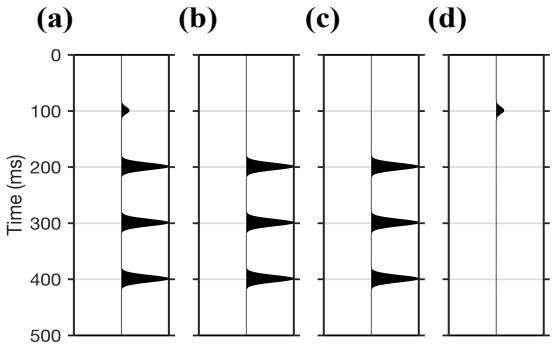

Figure 1: Illustration of the basic steps involved in adaptive subtraction (AS): (a) **D** is seismic data with one weak reflection and three high-amplitude surface waves; (b) $\mathbf{D}^{\mathbf{sw}}$ is the surface-waves part of Figure 1a; (c) $\mathbf{fD}^{\mathbf{sw}}$ results from convoluting the estimated shaping filter **f** with Figure 1b; (d) $\mathbf{D}^{\mathbf{refl}}$ is data after surface-waves suppression.

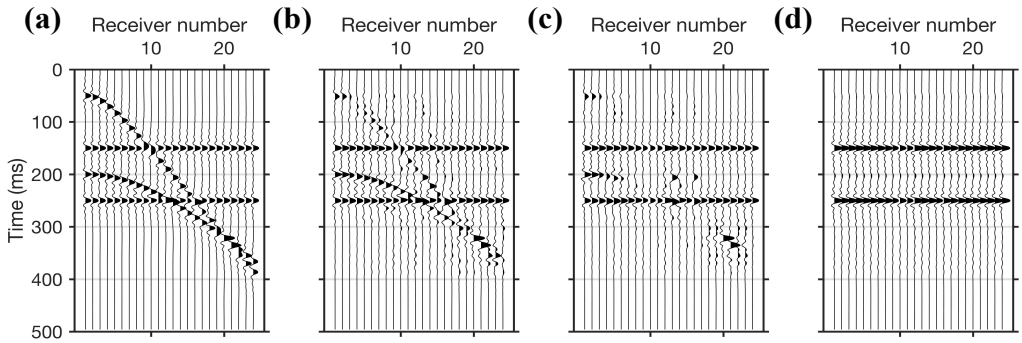

Figure 2: Illustration of the steps necessary to isolate horizontal arrivals from the seismic reflection shot gather using singular value decomposition (SVD) filtering: (a) synthetic seismic data (representing matrix **C**) with two horizontal noise events; (b-d) the low-rank matrix $\mathbf{C}_\mathbf{j}$ of **C**, by setting j to 12, 6, and 2, respectively.

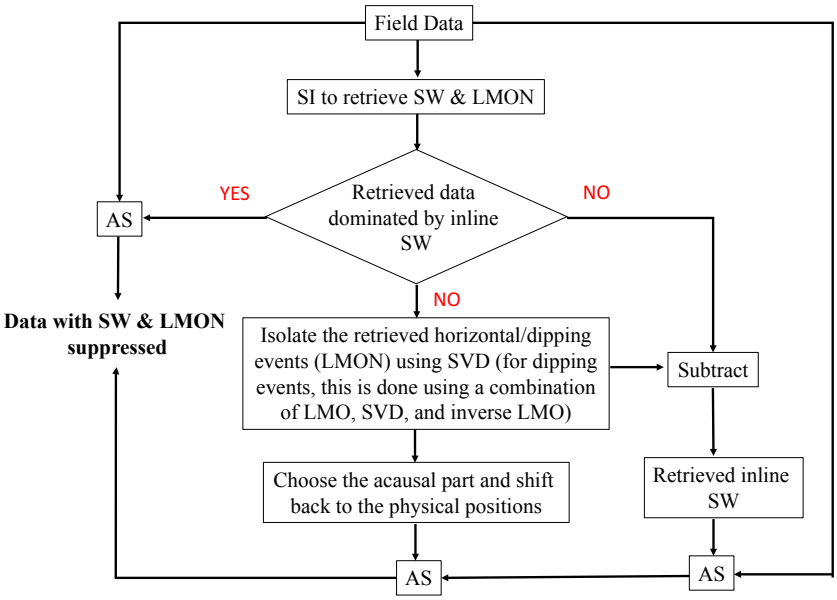

Figure 3: Flowchart for the implementation of seismic interferometry and adaptive subtraction (SI+AS) schemes to suppress source-coherent surface waves (SW) and linear moveout noises (LMON).

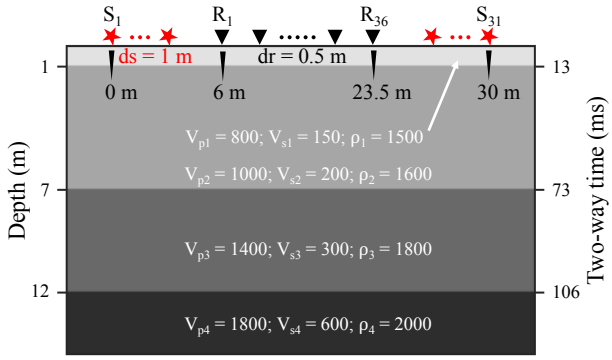

Figure 4: Model used to generate synthetic shot gathers. The units for V_p, V_s, and ρ are m/s, m/s, and kg/m^3, respectively. The acquisition geometry used for the synthetic studies is illustrated at the top of the model. The red stars represent sources, while the black triangles are receivers. The depth of each interface and its corresponding shear-wave reflection two-way time, are shown on left and right vertical axis, respectively.

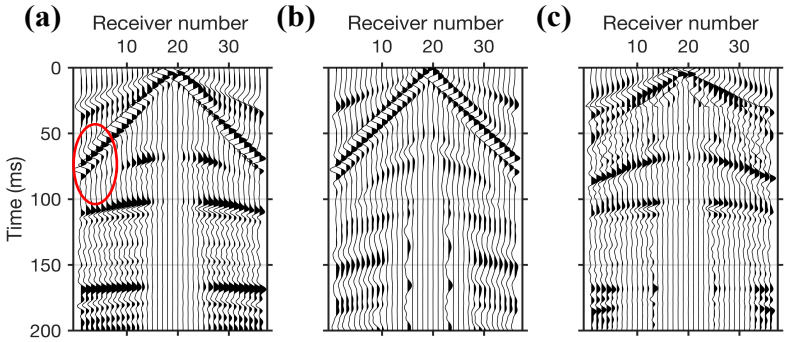

Figure 5: Steps for the implementation of the SI+AS scheme to suppress source-coherent surface waves: (a) a synthetic shot gather from the source located at 15 m; (b) retrieved virtual common-source gather using SI, with virtual source positioned at 15 m; (c) result after AS of the data in Figure 5b from the data in Figure 5a. The red ellipse highlights the area where the surface waves overlaps the reflection. For a better visualisation of events, an automatic gain control (AGC) with a window length of 50 ms is applied to the shot gathers. This same AGC is also applied to all other synthetic shot gathers presented in the following illustrations.

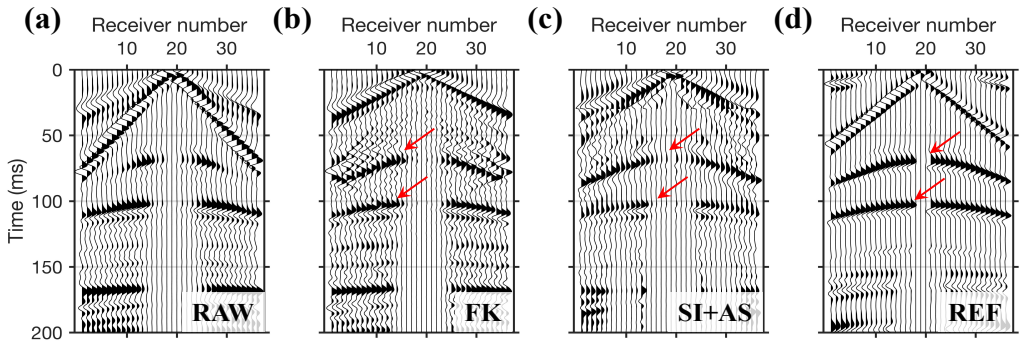

Figure 6: Comparison between the shot gather as in Figure 5a and the results after the application of f-k filtering and after SI+AS: (a) raw data as in Figure 5a; (b) result after f-k filtering; (c) result after SI+AS; (d) corresponding reference gather modelled without surface wave. The red arrows mark the primary shear-wave reflections from the interfaces of the model (at depth 7 m and 12 m), shown in Figure 4.

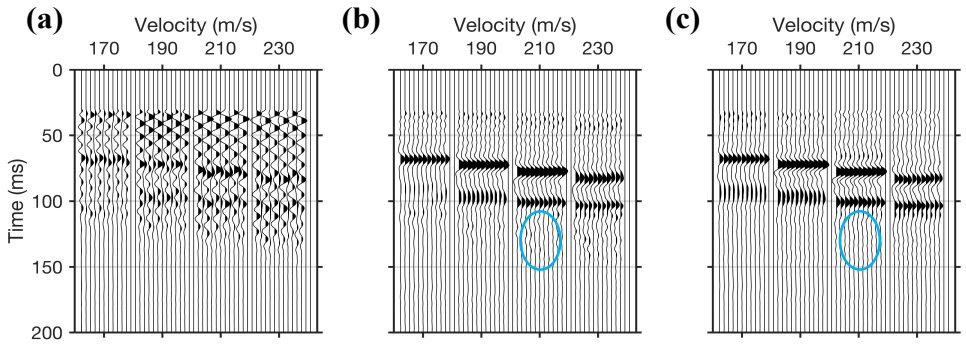

Figure 7: Comparison between constant velocity stacks (CVSs) from the raw data, data after f-k filtering, and data after SI+AS: (a) CVS section from the data as in Figure 6a without removal of surface waves; (b) CVS section after f-k filtering; (c) CVS section after SI+AS. For the CVS sections (e.g., Figure 7a), each subpanel shows a part of the stacked section, located from 14 m to 16.5 m in the model, obtained from stacking with different velocity labelled above the x-axis. The CVS sections (also the stacked sections in the following synthetic studies) are displayed without AGC, but after top muting the part above 30 ms. The blue ellipse highlights noise in Figure7b that has a higher amplitude than in Figure 7c.

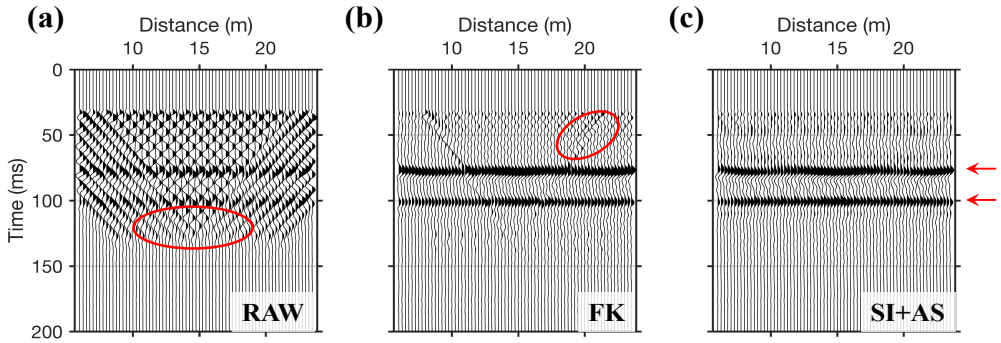

Figure 8: Comparison between stacked sections (located from 6 m to 23.5 m), from the raw data, data after f-k filtering, and data after SI+AS: (a) stacked section from data as in Figure 6a without removal of surface waves; (b) stacked section after f-k filtering; (c) stacked section after SI+AS. The areas highlighted by red ellipses are caused by stacking

of surface waves. We indicate the theoretical shear-wave two-way time from the second and third reflectors of the model in Figure 4 with red arrows on the right side of the panels.

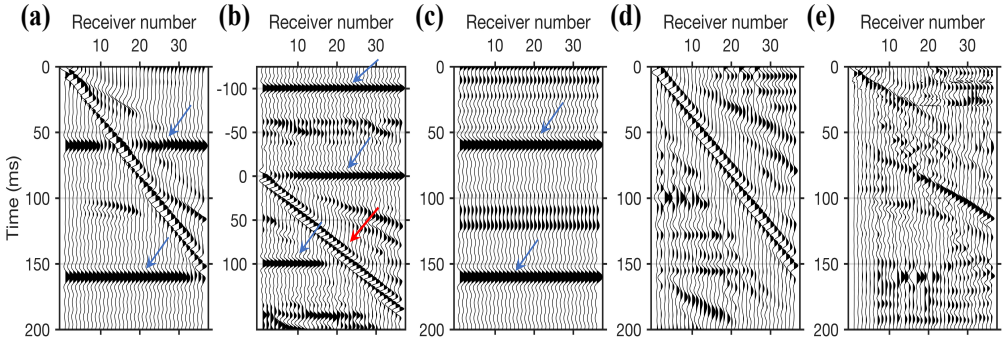

Figure 9: Steps for the implementation of the SI+AS to suppress source-coherent surface waves and horizontal linear moveout noises (LMON): (a) a synthetic shot gather for a source located at 6 m, where the blue arrows mark the horizontal LMON; (b) retrieved virtual common-source gather using SI for a virtual source located at 6 m, where the blue and red arrows indicate the retrieved horizontal LMON and the retrieved inline surface waves, respectively; (c) retrieved horizontal arrivals that are isolated using SVD and then manually moved to the time of the corresponding events in Figure 9a; (d) retrieved inline surface waves extracted from Figure 9b through subtraction of the retrieved horizontal LMON; (e) result after AS of the data in Figure 9c and Figure 9d from the data in Figure 9a.

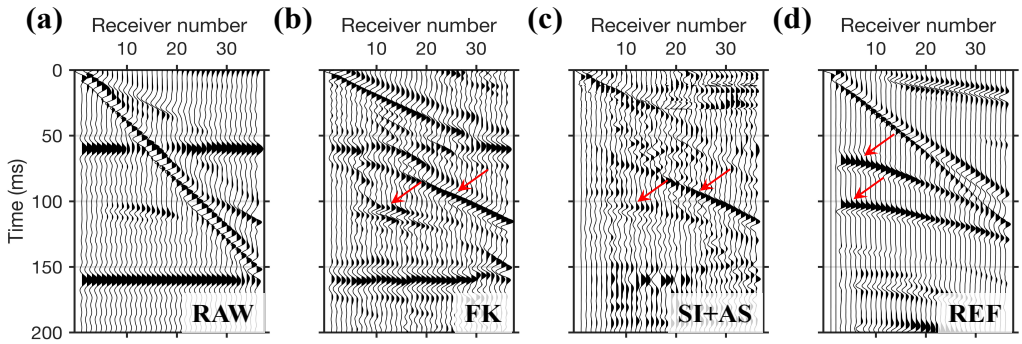

Figure 10: As in Figure 6, but in case of suppression of both source-coherent surface waves and horizontal linear moveout noises. The red arrows indicate the reflections from the interfaces of the model (Figure 4) at depths of 7 m and 12 m.

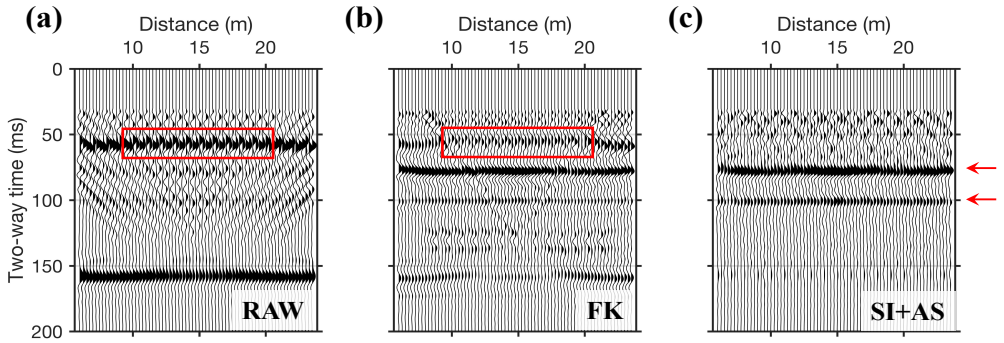

Figure 11: As in Figure 8, but for the data with source-coherent surface waves and horizontal linear moveout noises (LMON). Red rectangles mark the artefacts caused by stacking LMON.

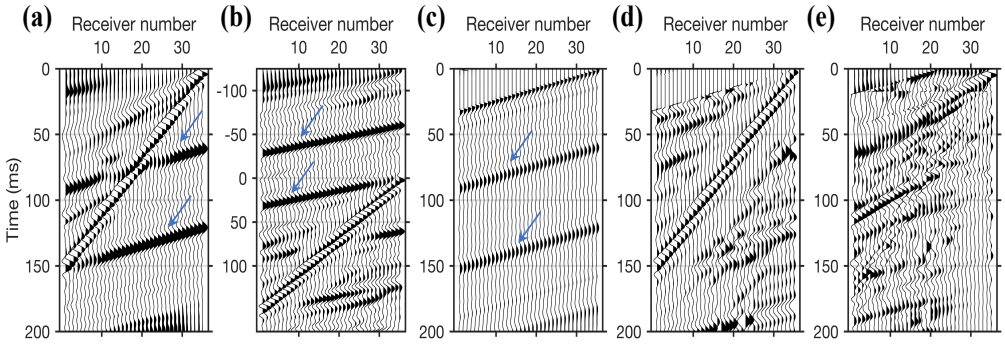

Figure 12: As in Figure 9, but in case of suppression of both source-coherent surface waves and dipping linear moveout noises (LMON). The active and virtual shot are at 24 m.

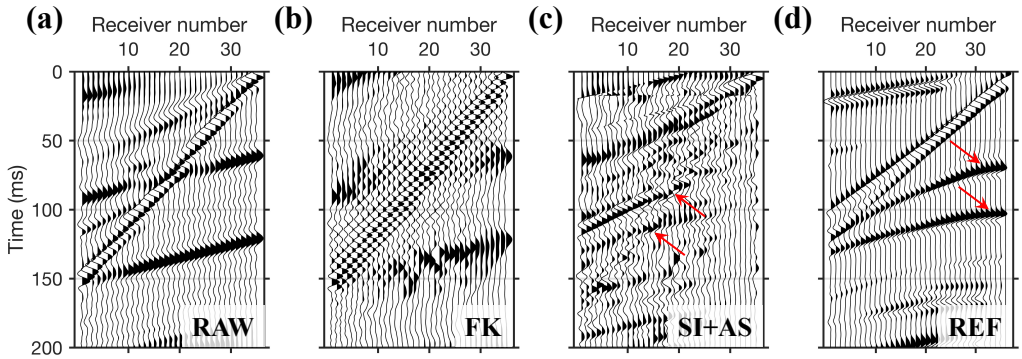

538

539 Figure 13: As in Figure 10, but in case of suppression of both source-coherent surface

540 waves and dipping linear moveout noises (LMON). The active and virtual shots are at 24

541 m.

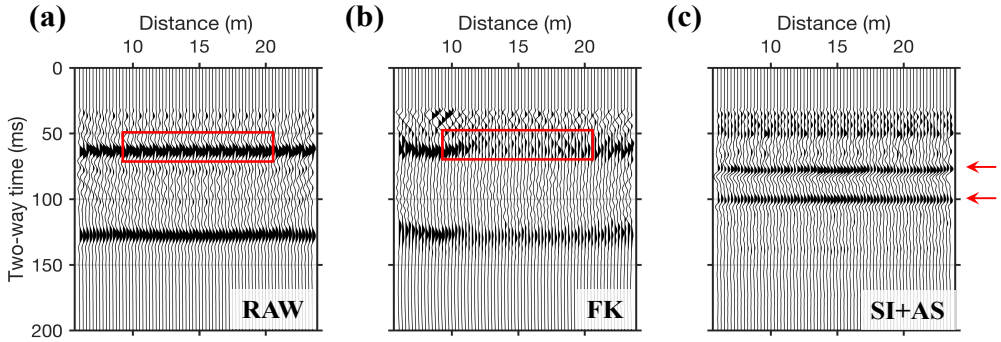

542

543 Figure 14: As in Figure 11, but for the data with source-coherent surface waves and

544 dipping linear moveout noises (LMON).

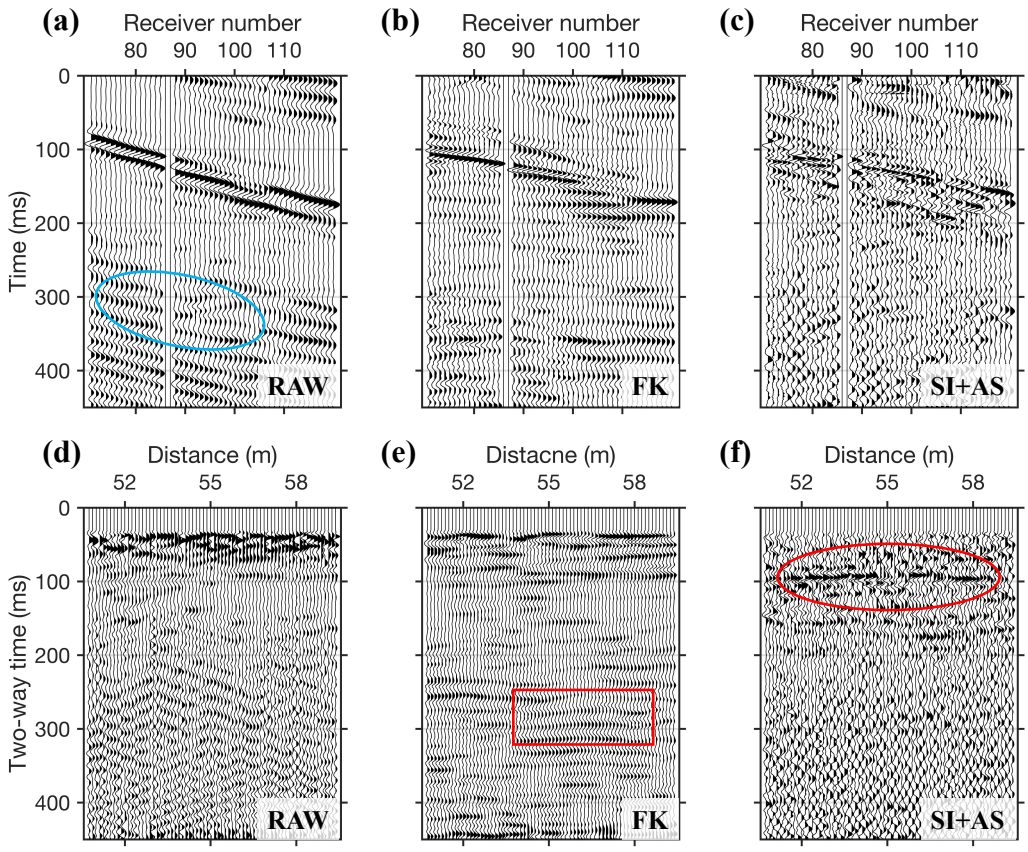

545

546 Figure 15: Comparison between field shear-wave shot gathers: (a) a typical raw shear-
547 wave shot gather acquired in the field contaminated by dipping linear moveout noises
548 (blue ellipse), with the source located at 50 m; (b) result after careful f-k filtering; (c)
549 result after SI+AS, following the procedure outlined in Figure 3. Comparison between
550 field shear-wave stacked sections: (d) using raw (unfiltered) field data; (e) using f-k
551 filtered data; (f) using SI+AS data. The red rectangle highlights the artefacts caused by f-
552 k filtering, whereas the red ellipse marks the revealed shallow reflectors via SI+AS.